PHYSICAL REVIEW C **88**, 065807 (2013)

Nuclear “pasta” formation

A. S. Schneider,[1,*] C. J. Horowitz,[1,†] J. Hughto,[1,‡] and D. K. Berry[2,§]
[1] *Department of Physics and Nuclear Theory Center, Indiana University, Bloomington, Indiana 47405, USA*
[2] *University Information Technology Services, Indiana University, Bloomington, Indiana 47408, USA*

(Received 8 July 2013; revised manuscript received 18 November 2013; published 20 December 2013)

The formation of complex nonuniform phases of nuclear matter, known as nuclear pasta, is studied with molecular dynamics (MD) simulations containing 51200 nucleons. A phenomenological nuclear interaction is used that reproduces the saturation binding energy and density of nuclear matter. Systems are prepared at an initial density of 0.10 fm^{-3} and then the density is decreased by expanding the simulation volume at different rates to densities of 0.01 fm^{-3} or less. An originally uniform system of nuclear matter is observed to form spherical bubbles (“swiss cheese”), hollow tubes, flat plates (“lasagna”), thin rods (“spaghetti”) and, finally, nearly spherical nuclei with decreasing density. We explicitly observe nucleation mechanisms, with decreasing density, for these different pasta phase transitions. Topological quantities known as Minkowski functionals are obtained to characterize the pasta shapes. Different pasta shapes are observed depending on the expansion rate. This indicates nonequilibrium effects. We use this to determine the best ways to obtain lower energy states of the pasta system from MD simulations and to place constraints on the equilibration time of the system.

DOI: 10.1103/PhysRevC.88.065807 PACS number(s): 26.60.Dd, 26.50.+x, 64.70.M−, 02.70.Ns

I. INTRODUCTION

During a supernova, the core of a massive star undergoes an extraordinary transformation, from 10^{55} separate nuclei to a single gigantic nucleus that forms the proto-neutron star. This transformation likely involves a series of nuclear pasta phase transitions that occur at densities somewhat below nuclear saturation density, $n_0 \simeq 0.16\ \text{fm}^{-3}$, and a range of exotic nuclear shapes. Knowing how matter organizes itself as its density increases from $n \lesssim 0.1 n_0$ to $\sim n_0$ has been a long standing problem in nuclear physics [1,2]. The description of nuclear matter at these subnuclear densities is relevant for a variety of problems such as determination of the structure and properties of neutron stars [1,3,4], the equation of state of nuclear matter [2,5], and neutrino transport in supernovae [6,7].

It is well established that at low densities, $n \lesssim 0.1 n_0$, attractive short-range strong interactions correlate nucleons into (almost) spherical nuclei. The size and shape of these nuclei are limited by Coulomb repulsion between protons and the surface energy of the system [8]. Also well established is the fact that at high densities, $n \gtrsim n_0$, nuclear matter saturates and becomes uniform. However, in between these two limits the picture is much less clear and considerable effort has been devoted to determine the phase transitions of matter as it goes from one extreme to the other.

Works using a liquid-drop model for the nuclei showed that a system with fixed temperature and proton fraction favors the formation of large nuclei, $Z > 100$, as the density increases [1,5]. Lamb *et al.* [5] then showed that when the fraction of volume occupied by nuclei reached $\sim 1/2$ matter would “turn inside out” and the system would then be composed of dense matter with bubbles of less-dense matter immersed in it. Later on, pioneering work by Ravenhall *et al.* [8] and Hashimoto *et al.* [9] showed that, at densities just below nuclear saturation density, matter organizes itself into other complex shapes besides spheres and spherical holes. This collection of shapes which includes rods, slabs, and cylindrical holes is caused by *frustration* of the system and is now referred to as *nuclear pasta*. The reason for frustration, the inability of a system to minimize all its fundamental interactions, is the competition between short-range nuclear attraction and long-range Coulomb repulsion [3].

Many works based on a compressible liquid-drop model [4,8–10] have explicit assumptions about the geometrical shapes of nuclear pasta. Some even include more exotic phases such as gyroid and double-diamond morphologies [11]. Approaches to the problem that do not explicitly assume any shape for the nuclear pasta have also been considered. They include calculations based on the Thomas-Fermi approximation [2,12–14], Hartree-Fock methods [15–17], density-functional theory [18], relativistic mean field approximation [10,19], quantum molecular dynamics (QMD) [20–26], and semiclassical molecular dynamics (MD) [6,7,27–30].

All the works described in the paragraph above conclude that matter just below nuclear saturation density forms unusual structures with geometrical shapes that depend on temperature, proton fraction, and density. Some of these works, mainly the ones using a liquid-drop model and Thomas-Fermi approximation, use a Wigner-Seitz cell approximation to determine the periodicity of the pasta shapes [4,8,10,11,14,18] while other works use a unit cell to account for the periodicity of the system [2,9,13,15–17]. Meanwhile, works based on QMD and MD methods use larger volumes and do not assume any periodicity in the pasta shapes besides the one imposed by periodic boundary conditions [6,7,20–30]. Still, some QMD simulations were able to achieve some degree of periodicity within their simulation volumes [23–26]. Recently Okamoto

---

[*] andschn@indiana.edu
[†] horowit@indiana.edu
[‡] jhughto@astro.indiana.edu
[§] dkberry@iu.edu

et al. used the Thomas-Fermi approximation to calculate pasta shapes not limited to a single unit cell [12] and also obtained periodic configurations smaller than their simulation volume.

One reason for so many studies on the pasta phase is its relevance for properties of neutron stars and core collapse supernovae. For example, neutrino-pasta scattering helps determine the neutrino opacity in core collapse supernovae [6,7]. This is because supernova neutrinos have wavelengths comparable to pasta sizes and can scatter coherently from the pasta. Furthermore, electron-pasta scattering is important for determining the shear viscosity, thermal conductivity [28] and electrical conductivity. The electrical conductivity of the pasta may be relevant for the decay of neutron star magnetic fields [31].

Possible hysteresis in pasta shapes with changes in density will contribute to the bulk viscosity. This could be important for the damping of collective r-mode oscillations of rapidly rotating neutron stars. The excitation spectrum is important for the pasta heat capacity; see also Ref. [27]. Meanwhile, the shear modulus of the pasta is important for the speed of shear waves and crustal oscillation frequencies of neutron stars. The breaking strain of the pasta helps determine the maximum sized mountain that can be supported on a neutron star [32]. It may also be relevant for star quakes and crust breaking models of magnetar giant flares. In general the strength increases with increasing density and, therefore, the pasta is expected to make a significant contribution to the strength of the neutron star crust because of its high density.

In the next sections, we will discuss some properties of the pasta phases at different densities obtained from molecular dynamics (MD) simulations. We use the molecular dynamics formalism of Horowitz *et al.* [6,7,27,28]. However, while their main focus was transport properties of the pasta, our focus here is the study of the equilibration mechanisms and the topological structures formed by the pasta phases as they transition from low to high densities. As the initial conditions are much simpler when the system is nearly uniform we start our simulations at high densities, near half the nuclear saturation density, and then slowly expand the simulation volume to obtain lower densities.

To study the pasta and its phase transitions it is helpful to provide some simple metrics that quantify their geometrical shapes. This can be achieved by making use of integral-geometric formulas [33] often referred to as Minkowski functionals [34]. Minkowski functionals are a robust way to describe complex structures. They were first used to describe the topology of nuclear pasta structures by Watanabe *et al.* in the context of quantum molecular dynamics [22,23,25]. More recently Dorso *et al.* calculated the Minkowski functionals for pasta structures obtained from classical molecular dynamics [30] while Schuetrumpf *et al.* did the same using a time-dependent Hartree-Fock approach [16].

In this work we use Minkowski functionals to quantify how the pasta shapes change as a function of the expansion rate. We believe this allows us to address some questions related to the equilibration time of the pasta and its transition from one phase to the other. A couple of papers by Watanabe *et al.* have already explored the mechanisms of pasta phase transitions and their equilibration or transition times using QMD [25,26]. In these papers Watanabe *et al.* started their simulations from low density and compressed the system adiabatically or isothermally to determine the time scale of transitions between different pasta shapes. As we will see the time scales they find using QMD are significantly faster than the ones we obtain with MD.

In this paper we use MD to simulate nuclear matter for densities of ~ 0.010 to $0.10\ \mathrm{fm}^{-3}$ for a proton fraction of $Y_p = 0.40$ at a temperature of $T = 1$ MeV. This temperature and proton fraction are roughly comparable to those in the collapsing dense core of a supernova, before the matter is heated further by a shock wave. We start Sec. II reviewing the formalism used to describe nucleon-nucleon interactions, Sec. II A, and then move on to explain the methods used to obtain the topological properties of the pasta, Sec. II B. In Sec. III we present the main results of our simulations with Sec. III A devoted to a description of our runs and Sec. III B to a discussion of how the topology of the pasta changes as a function of density. We conclude in Sec. IV.

II. FORMALISM

In Sec. II A we review our MD simulation formalism. Section II B is devoted to the methods used to obtain the topology of the pasta while Sec. II C describes an algorithm to determine which nucleons belong to which nuclei.

A. Semiclassical nuclear pasta model

Here we briefly describe the formalism used in our MD simulations. It is essentially the same as the one used by Horowitz *et al.* and others in previous works [6,7,27–30]. The simulated systems are composed of neutrons, protons and electrons. The electrons are assumed to be noninteracting and, thus, are described as a degenerate free Fermi gas. Meanwhile, the nucleons are treated as mass $M = 939$ MeV point-like particles that interact via an "elementary" two-body force. The interaction between any two nucleons i and j can be separated into nuclear, v_{ij}^n, and electromagnetic (Coulomb) v_{ij}^c, components; that is

$$v_{ij} = v_{ij}^n + v_{ij}^c. \tag{1}$$

The nuclear component of the interaction is

$$v_{ij}^n = a e^{-r_{ij}^2/\Lambda} + [b + c\tau_z(i)\tau_z(j)]\, e^{-r_{ij}^2/2\Lambda}. \tag{2}$$

Here, $r_{ij} = |\boldsymbol{r}_i - \boldsymbol{r}_j|$ is the distance between particles i and j and $\tau_z = +1$ (-1) is the isospin projection of the particle if it is a proton (neutron). The constants a, b, c, and Λ describing the two-body potential are the same ones used in Ref. [6]. Their values are given in Table I and were adjusted to

TABLE I. Nuclear interaction parameters. The parameter a defines the strength of the short-range repulsion between nucleons, b and c the strength of their intermediate-range attraction, and Λ the length scale of the nuclear potential.

a (MeV)	b (MeV)	c (MeV)	Λ (fm^2)
110	−26	24	1.25

approximately reproduce some bulk properties of pure neutron matter and symmetric nuclear matter as well as the binding energies of selected nuclei. This parametrization predicts a value $L = 40.7$ MeV for the nuclear symmetry energy and $K = 372$ MeV for the nuclear compressibility.

The Coulomb component of the interaction is

$$v_{ij}^c = \frac{\alpha}{r_{ij}} e^{-r_{ij}/\lambda} \tau_p(i) \tau_p(j), \tag{3}$$

where α is the fine structure constant, $\tau_p \equiv (1 + \tau_z)/2$ the nucleon charge, and λ is the screening length that results from the slight polarization of the background electron gas [35]. The relativistic Thomas-Fermi screening length is given by

$$\lambda = \frac{\pi^{1/2}}{2\alpha^{1/2}} \left(k_F \sqrt{k_F^2 + m_e^2} \right)^{-1/2} \tag{4}$$

where $k_F = (3\pi^2 n_e)^{1/3}$ is the Fermi momentum of the electrons with n_e the electron density and m_e the electron mass. However, to be consistent with previous works, we fix λ at a constant value $\lambda = 10$ fm. This is somewhat smaller than Eq. (4) and allows us to decrease the size of our simulations without introducing large finite-size effects.

All of our simulations have a fixed number of particles $N = 51\,200$, a proton fraction of $Y_p = 0.40$, and a temperature of $T = 1$ MeV. We use periodic boundary conditions where a nucleon interacts only with the nearest periodic image of the other nucleons. We also use a cutoff radius of 8λ for the Coulomb part of the potential and 11.5 fm for the nuclear potential. Both potentials are assumed to be zero for distances larger than their cutoff radius.

Knowing the positions of each particle along with the interparticle potentials allows us to calculate the total force on each nucleon. The new particle positions and velocities are then obtained using a velocity Verlet algorithm [36]. After every time step Δt we increase each side l_i of the box $(i = x, y, z)$ by $\Delta l = l_i(0)\dot{\xi}_i \Delta t$. That is, the side l_i of the box at a time t is

$$l_i(t) = l_i(0)(1 + \dot{\xi}_i t) \tag{5}$$

where $l_i(0)$ is the initial length of the box and $\dot{\xi}_i$ is the expansion rate along direction i. Since in all of our simulations the boxes are assumed to be cubic and the expansion rates are assumed to be the same along every direction we will omit the subscript i from now on. Particle positions are not adjusted artificially, but rather are allowed to respond dynamically to the changing simulation volume. Also, particle velocities are unaffected by the stretching. This contrasts with Ref. [37] where the velocities of particles are affected by the expansion rate and periodicity of the system. As explained in the next paragraph, our choice to not rescale the velocities to account for the expanding periodic boundary conditions should not affect the dynamics of the system due to the strong overall binding of particles in our system, the slow expansion rates ($\dot{\xi} \leqslant 10^{-5}$ c/fm), and temperature ($T = 1$ MeV) that we used.

As discussed by Holian and Grady in Ref. [37], Newton's laws for an expanding system with periodic boundary conditions imply that the velocities of particles that leave the box on one side and reenter the box on the other side are affected by the expansion of the box. The contribution that should be added to or subtracted from the total velocity of the particle as it crosses one of the box boundaries is of order $\dot{l} = l_0\dot{\xi}$. However, since the temperature $T = 1$ MeV used in our simulations implies an average velocity for nucleons of 0.057 (in units of $c = 1$), the correction $\dot{l}$ to the velocities of particles that cross any of the box boundaries would be on average of order 1.4% for the fastest expansion rate used in this work, $\dot{\xi} = 10^5$ c/fm. Though we expect such small corrections to not affect the dynamics of the system, in future works they should be implemented into our algorithm.

TABLE II. Minkowski functionals in three dimensions, adapted from Ref. [16]. K is the domain where the functionals are evaluated while κ_1 and κ_2 are the principal curvatures on ∂K.

V	Volume
$A = \int_{\partial K} dA$	Surface area
$B = \int_{\partial K} (\kappa_1 + \kappa_2)/4\pi \, dA$	Mean breadth
$\chi = \int_{\partial K} (\kappa_1 \kappa_2)/4\pi \, dA$	Euler characteristic

B. Topology

A powerful and general method to quantify the topological structures present in a system is provided by the Minkowsky functionals. In N dimensions there are $N + 1$ Minkowski functionals which completely describe the morphological properties of an object. In three dimensions the Minkowski functionals are quantities proportional to the volume V, surface area A, mean breadth B, and Euler characteristic χ; see Table II.

Though there are four Minkowski functionals, two are sufficient to characterize the shapes of the pasta: the mean breadth B and the Euler characteristic χ. The mean breadth B is a measure of the average curvature of the structures that form the pasta and is proportional to the surface integral of the mean curvature $(\kappa_1 + \kappa_2)/2$. Here, κ_1 and κ_2 are the principal curvatures on the surface ∂K that defines the pasta. Recall that for a concave system the curvatures are negative while for convex systems the curvatures are positive. The Euler characteristic χ, though proportional to the surface integral of the Gaussian curvature $(\kappa_1\kappa_2)$, is related to the number of structures in the system. In the three-dimensional case it can be shown to be given by the number of connected components plus the number of cavities minus the number of tunnels in the system [34], that is,

$$\begin{aligned} \chi = &\,(\text{no. connected components}) \\ &+ (\text{no. cavities}) - (\text{no. tunnels}). \end{aligned} \tag{6}$$

The eight possible structures according to their curvatures are discussed in Table III. For images of these structures see Fig. 1 of Ref. [16].

In our simulations we considered nucleons to be point particles. However, this makes the problem of calculating the four Minkowsky Functionals intractable as point particles do not define a surface. To circumvent this we change our treatment of the particles from point-like to normal distributions centered at the position determined by the simulations. Thus, the number density of a nucleon i and, similarly, the charge density of a

TABLE III. Description of the possible pasta phases according to the values of the mean breadth B and Euler characteristic χ, adapted from Refs. [16,30]. Shapes include nearly spherical nuclei (sph), three cylindrical or spaghetti phases classified according to their connectivity (rod-1, -2, and -3), a flat sheet phase (slab), two hollow-tube or anti-spaghetti phases (rod-1 b and rod-2 b), and a nearly spherical bubble phase (sph b).

	$B < 0$	$B \sim 0$	$B > 0$
$\chi > 0$	sph b		sph
$\chi \sim 0$	rod-1 b	slab	rod-1
$\chi < 0$	rod-2 b	rod-3	rod-2

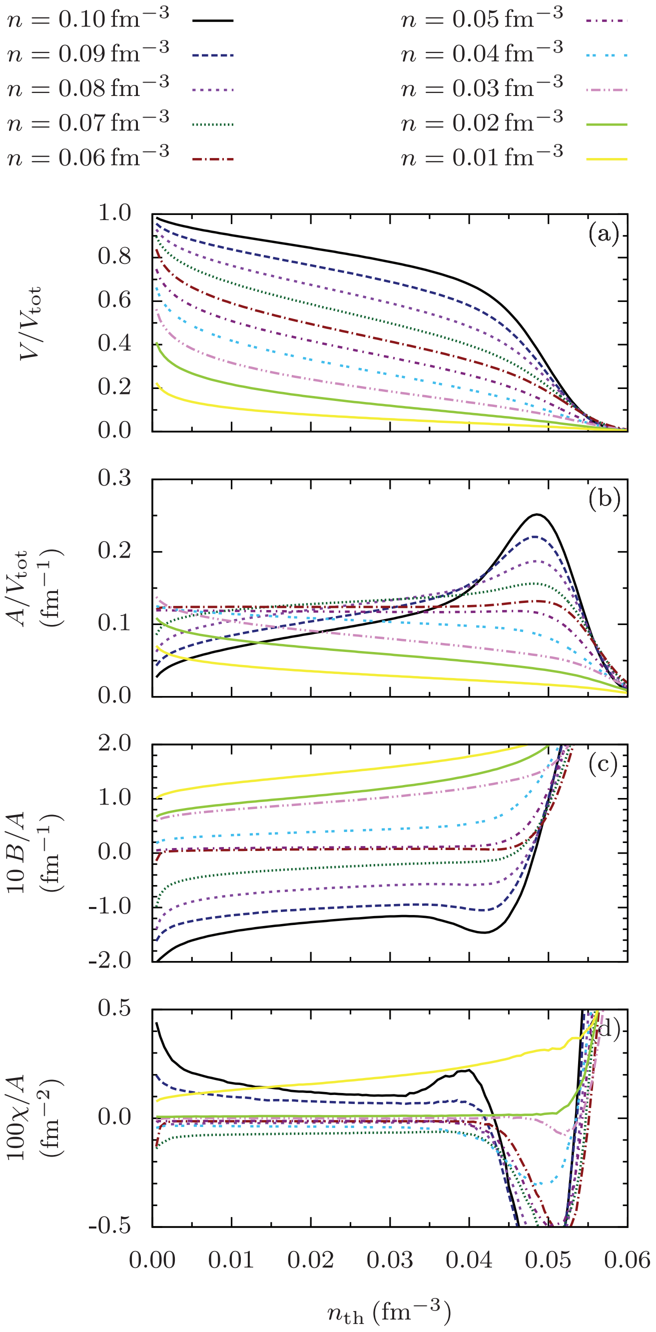

FIG. 1. (Color online) Normalized Minkowski functionals as a function of the threshold charge density n_{th} for systems at ten different nucleon densities n indicated by the lines at the top. Configurations analyzed were obtained by stretching the pasta system from 0.10 to 0.01 fm^{-3} at a rate of $\dot{\xi} = 1.0 \times 10^{-7}$ c/fm. From top to bottom the figures show (a) occupied volume fraction V/V_{tot}, (b) surface area per unit volume A/V_{tot}, (c) average mean curvature B/A, and (d) average Gaussian curvature χ/A.

proton transform as

$$\delta(\boldsymbol{r} - \boldsymbol{r}_i) \to \frac{1}{(2\pi\sigma)^{3/2}} \exp\left(-\frac{(\boldsymbol{r} - \boldsymbol{r}_i)^2}{2\sigma^2}\right), \qquad (7)$$

where σ is the standard deviation of the distribution.

With this in mind we follow the recipe laid out by Lang*et al.* [33] to obtain the four Minkowski functionals. A short explanation of the method follows.

We start by dividing each side $l(t)$ of our cubic system into n segments of edge length Δ, that is, $l(t) = n\Delta$. Now that the system has been divided into n^3 cubes with vertices at $\boldsymbol{r} = (i\Delta, j\Delta, k\Delta)$ with $i, j, k = 0, \ldots, n-1$, we fold a Gaussian over each proton to determine the charge density n_{ijk} at the vertex of each cube. Our choice for charge density over nuclear density was made as there is more contrast in the former than the latter. If the charge density n_{ijk} is larger than a predefined threshold value n_{th} that vertex is considered occupied and assigned a value $b_{ijk} = 1$. Otherwise the vertex is considered unoccupied and $b_{ijk} = 0$. Thus, we have a discrete binary image of our system.

Once all voxels, values of b_{ijk}, are determined we analyze its $2 \times 2 \times 2$-neighborhood configuration. The neighborhood consists of eight voxels: b_{ijk}, b_{ij+1k}, b_{ijk+1}, $b_{ij+1k+1}$, b_{i+1jk}, $b_{i+1j+1k}$, $b_{i+1jk+1}$, and $b_{i+1j+1k+1}$. Due to our choice of periodic boundary conditions if $i = n-1$ then $i+1 = 0$. The same is valid for j and k. This analysis consists of applying a filter to determine the grey-tone g_{ijk} of each voxel. The filter is chosen so that $g_{ijk} = \sum_{l,m,n=0}^{1} 2^{l+2m+4n} b_{i+l,j+m,k+n}$. While the voxels b_{ijk} define a 2-bit image as $b_{ijk} = 0$ or 1 the grey-tones g_{ijk} compose an 8-bit image as g_{ijk} can assume any value from 0 to 255. A simple histogram h_l of the values of g_{ijk} is enough to obtain the four Minkowski functionals. For example, the occupied volume V of the system is simply given by

$$V = \Delta^3 \sum_{l=0}^{127} h_{2l+1} \qquad (8)$$

while the Euler characteristic χ is given by

$$\chi = \Delta^3 \frac{\pi}{6} \sum_{l=0}^{255} \nu_l h_l \qquad (9)$$

for a suitable choice of vector ν_l. For a more in-depth discussion and expressions for the surface area A and the mean breadth B see Ref. [33].

In our analysis we set the value of σ, which can be thought of as the nucleon radius, to 1.5 fm. Though this value for σ may seem rather large, it fulfills our main requirement described below. At low densities, $n \lesssim 0.010\ \mathrm{fm}^{-3}$, the system forms clusters that can be identified to be (almost) spherical nuclei. We want these clusters to be bound by a single isosurface with $n = n_{\mathrm{th}}$ and all regions inside those isosurface to have $n > n_{\mathrm{th}}$. If σ is too small, our algorithm will find regions of low charge density inside the clusters, which would be equivalent to holes inside a nucleus. We clearly should avoid that when determining the topology of the system. Moreover, we want the value of χ in Eq. (6) to match the number of clusters determined by the MST algorithm discussed in Sec. II C, and this depends on a fine tuning of σ and n_{th}.

Next we determine the threshold charge-density isosurface n_{th} which will be used to to obtain the Minkowski functionals. A comparison of normalized values for the four Minkowski functionals as a function of n_{th} for one of our simulations is shown in Fig. 1. The volume V and surface area A were normalized to the total volume of the system V_{tot} while the mean breadth B and the Euler characteristic were normalized to the total surface area A. The procedure described by Michielsen and De Raedt in Ref. [34] was shown to provide somewhat similar qualitative (though quantitatively different) results for our choice of σ.

In order to chose a value for n_{th} we describe what sort of behavior we expect from the topology analysis of a low density system, $n \lesssim 0.010\ \mathrm{fm}^{-3}$. We want n_{th} small enough that at these low densities, when nuclei can be clearly separated from each other, the charge isosurfaces $n = n_{\mathrm{th}}$ determines a closed surface that contains all of the protons in a given cluster. However, n_{th} should also be large enough so that none of the protons in nearby clusters are contained within these isosurfaces. Both requirements are equivalent to matching at low densities the number of clusters N_{clusters} obtained from the MST algorithm described in Sec. II C to the value of χ obtained from the analysis described in this section. For these reasons we choose a threshold proton density of $n_{\mathrm{th}} = 0.030\ \mathrm{fm}^{-3}$ as this value satisfies the above requirement, $N_{\mathrm{clusters}} = \chi$ at low densities, within 2% or less. This value also makes the nuclei surfaces smooth enough that the Minkowski functionals converge for $\Delta \lesssim 0.5$ fm using the method outlined above. We note that this procedure contrasts with the work of Watanabe *et al.* in Ref. [22] where they choose the isosurface $n = n_{\mathrm{th}}$, which defines the shape of nuclear structures, to be based on nuclear density and as a function of the quantities A and V.

C. Cluster algorithm

Now we explain two algorithms, MST and MSTE, used to determine the number of neutrons and protons in each cluster formed in the system. The first algorithm is very similar to the standard “minimum spanning tree” (MST) described in Refs. [7,30,38] while the second one is the “minimum spanning tree in two-particle energy space” (MSTE) described in Ref. [38].

Our MST algorithm starts by looking for correlations in coordinate space between the positions of protons. A proton i is said to be part of a cluster C if it is within a cutoff distance r_{pp} of at least one proton j that is part of C. That is, if nucleons i and j are protons then $i \in C$ if and only if $\exists j \in C$ such that $|\boldsymbol{r}_i - \boldsymbol{r}_j| \leqslant r_{pp}$. Note that, to take into account the periodicity of the system, the distance $|\boldsymbol{r}_i - \boldsymbol{r}_j|$ is defined as the distance between proton i and the closest periodic image of proton j. We set $r_{pp} = 4.5$ fm as this is is very close to the first nonzero minimum of the proton-proton correlation function $g_{pp}(r)$. Note that the position of this minimum does not appear to depend on the density of the system, as can be seen on Fig. 2(a).

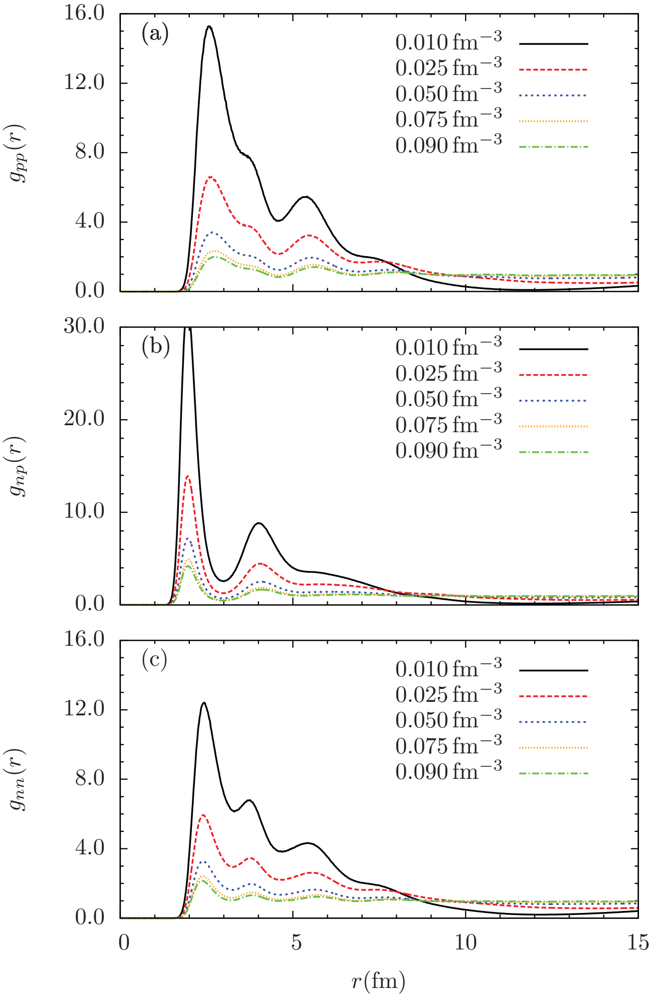

FIG. 2. (Color online) Nucleon pair-pair autocorrelation function as a function of pair distance for our five constant-density runs. See Sec. III A for description of the five runs. From top to bottom the plots show (a) proton-proton correlations $g_{pp}(r)$, (b) neutron-proton correlations $g_{np}(r)$, and (c) neutron-neutron correlations $g_{nn}(r)$.

After separating the protons into clusters we count the neutrons in each of the clusters. We say a neutron is part of cluster C if it is within a distance r_{np} of at least one proton j that is part of C. That is, if i is a neutron and j is a proton then $i \in C$ if and only if $\exists\, j \in C$ such that $|\boldsymbol{r}_i - \boldsymbol{r}_j| \leqslant r_{np}$. Again the periodicity of the system is taken into account by defining $|\boldsymbol{r}_i - \boldsymbol{r}_j|$ as the smallest distance between neutron i and all the periodic images of proton j. We set the cutoff distance $r_{np} = 3$ fm, approximately the first nonzero minimum of the neutron-proton correlation function $g_{np}(r)$ as seen on Fig. 2(b). For completeness we also plot the neutron-neutron correlation function $g_{nn}(r)$ on Fig. 2(c). Neutrons that are not part of any cluster are considered free neutrons.

The MSTE algorithm looks for correlations in two-particle energy space and works the following way: for any pair of nucleons i and j nucleon $i \in C$ if and only if $\exists\, j \in C$ such that $e_{ij} < 0$. Here, the two-particle energy e_{ij} is defined as $e_{ij} = v_{ij} + |\boldsymbol{p}_i - \boldsymbol{p}_j|/4\mu$, where μ is the reduced mass of nucleons i and j. This method, thus, takes into account the relative momenta of nucleons when determining whether they are part of a cluster or not. As will be shown in Sec. III B5, we obtain similar results with both algorithms.

As noted by Dorso *et al.* in Ref. [30], the low temperatures and small momentum transfers in stellar crusts guarantee that the MST and MSTE algorithms yield accurate results for the clusterization of the system. Thus, they are preferred over more robust algorithms such as the "early cluster recognition algorithm" (ECRA), which takes into account relative momenta and binding energies beyond two particles [39].

III. RESULTS

This section is devoted to the results of our simulations. In Sec. III A we detail the initial conditions and aspects of the different runs performed using the MD formalism. Meanwhile, in Sec. III B we describe the differences in pasta shapes at densities of 0.010, 0.025, 0.050, 0.075, and 0.090 fm^{-3} according to the type of simulation from which they were obtained. We finish the section with a comparison of the Minkowski functionals as a function of density followed by a discussion of the equilibration time of the pasta.

A. Simulations

Every simulation described here has 51 200 particles, a proton fraction $Y_p = 0.40$, and is evolved at a temperature of 1 MeV. Two types of simulation were performed in this work: stretching or expansion runs and constant-density runs.

For all of our expansion runs we set an initial density of 0.10 fm^{-3}. This makes our initial simulation volume a cube 80 fm on a side. Each particle is given an initial random position inside the box and a velocity randomly selected from a Boltzmann distribution such that its temperature is 1 MeV. The system is equilibrated at constant density for a total time of 10 000 fm/c using a time step of $\Delta t = 1$ fm/c. The temperature is kept approximately constant by rescaling the velocities of nucleons every one hundred time steps. Though the topological characteristics of these short equilibration runs do not change much after 10 000 fm/c compared to much longer runs, 500 000 fm/c, it is not clear whether the system has equilibrated. Further simulations, possibly starting at nuclear saturation density or above and slowly expanded to 0.10 fm^{-3}, are needed in order to study the equilibrium configuration of the system. This will be done in future works.

After the short equilibration time the final configuration is evolved using three different stretching rates, $\dot{\xi} = 10^{-5}$, 10^{-6}, and 10^{-7} c/fm, until it reaches a density slightly lower than 0.010 fm^{-3}. Like in the equilibration phase, the temperature during the expansion is also kept approximately constant by rescaling the velocities every one hundred time steps. Though this simple choice was made solely in order to avoid the temperature from drifting away from the desired temperature, later simulations showed that temperature rescaling was not necessary to keep the temperature close to its desired value; see Table IV. For the two fastest stretching rates, $\dot{\xi} = 10^{-5}$ and 10^{-6} c/fm, the temperature drift was very small. In the worse-case scenarios, temperature drifts were less than 1 part in 1 000 for a time scale of order $\dot{\xi}^{-1}$. We expect the same to hold true for even slower stretch rates.

TABLE IV. Linear fit parameters, $T(t) = \alpha + \beta t$, for the temperature as a function of time for systems stretched at rates $\dot{\xi} = 10^{-5}$ and 10^{-6} c/fm. In every fit $\alpha = 1$ within 1 part in 1 000 or less and β and its percentage error are shown below. The fits were performed for four different frequencies of temperature rescaling $\Delta t_{\mathrm{norm}} = 1$, 100, 10 000, and ∞ (no rescaling performed). The values for β and its uncertainty show that $T(t)$ is consistent with $T = 1$ MeV for the time scales of the runs, $(\dot{\xi})^{-1}$.

$\dot{\xi}$ (c/fm)	Δt_{norm} (fm/c)	β (10^{-10} MeV c/fm)	$\Delta\beta/\beta$ (%)
10^{-5}	1	−1.04829	197.1
10^{-5}	100	32.8097	57.62
10^{-5}	10 000	5.94086	119
10^{-5}	∞	20.3109	33.1
10^{-6}	1	−0.286657	184.2
10^{-6}	100	−0.914527	186.7
10^{-6}	10 000	2.16478	81.52
10^{-6}	∞	0.491453	370

During the runs an output file with the positions and velocities of all particles in the system is written every 1000 fm/c and its topological characteristics, as explained in Sec. II B, are obtained. An expansion run without the Coulomb interaction and a stretching rate of $\dot{\xi} = 1.0 \times 10^{-6}$ c/fm was also performed following the same procedure as the runs described above.

Five constant-density runs were performed at fixed densities of 0.010, 0.025, 0.050, 0.075, and 0.090 fm^{-3}. Initially we assign each particle a random position inside a cubic box with sides $l = \sqrt[3]{N/n}$. Each particle is also given an initial velocity randomly selected from a Boltzmann distribution such that the system has a temperature close to 1 MeV. The system is evolved at constant density for a total time of 500 000 fm/c using a time step of 1 fm/c. The velocities of the nucleons are rescaled every one hundred time steps to keep a 1 MeV temperature. The topological characteristics of the system are obtained every 1000 fm/c for the last 100 000 fm/c of the run and are observed to not change significantly during that time.

With the exception of our slowest expansion run, $\dot{\xi} = 1.0 \times 10^{-7}$ c/fm, all of our simulations were performed on the BigRed supercomputer at Indiana University using typically 128 cores for a few days to about a week. The expansion run with $\dot{\xi} = 1.0 \times 10^{-7}$ c/fm was performed on the Kraken supercomputer [40] using about 1152 cores for a total of about 150 hours.

B. Discussion

In Fig. 3 we compare the isosurfaces of charge density for four different runs at densities of 0.010, 0.025, 0.050, 0.075, and 0.090 fm^{-3}. For the constant-density run we show the

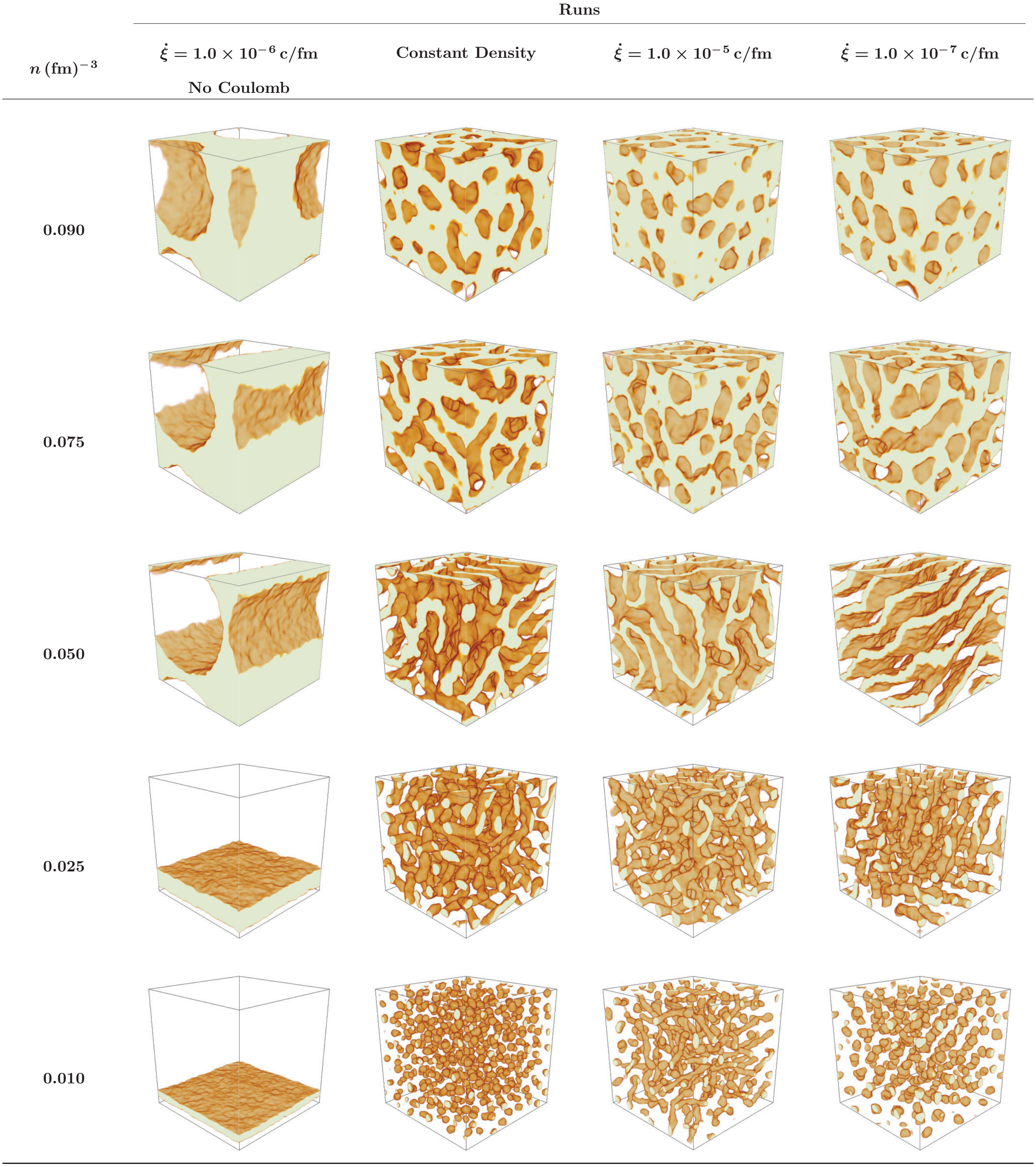

FIG. 3. (Color online) Side by side comparison of charge density isosurfaces of configurations with densities of 0.010, 0.025, 0.050, 0.075, and 0.090 fm^{-3} obtained from four different runs. The golden surfaces represent isosurfaces of charge density with $n_{\mathrm{ch}} = 0.03\ \mathrm{fm}^{-3}$ while the cream color shows regions such that $n_{\mathrm{ch}} > 0.03\ \mathrm{fm}^{-3}$. The first "Runs" column shows configurations obtained neglecting Coulomb interactions while the second Runs column shows constant density runs. Finally, the third and fourth Runs columns show respectively configurations obtained with the fastest stretching rate, $\dot{\xi} = 1.0 \times 10^{-5}\ \mathrm{fm}/c$, and the slowest stretching rates, $\dot{\xi} = 1.0 \times 10^{-7}\ \mathrm{fm}/c$. This figure was generated using PARAVIEW [41].

isosurfaces obtained for the configuration at 500 000 fm/c. For the two stretching runs including Coulomb potential, $\dot{\xi} = 1.0 \times 10^{-5}\ c/\mathrm{fm}$ and $\dot{\xi} = 1.0 \times 10^{-7}\ c/\mathrm{fm}$, and for the run that does not include the Coulomb potential, $\dot{\xi} = 1.0 \times 10^{-6}\ c/\mathrm{fm}$,

TABLE V. Values for the normalized mean breadth B/A for our simulations at densities of 0.010, 0.025, 0.050, 0.075, and 0.090 fm^{-3}.

n	B/A (fm^{-1})			
(fm^{-3})	No Coulomb	Constant	$\dot{\xi} = 10^{-5}$	$\dot{\xi} = 10^{-7}$
0.090	-2.7×10^{-2}	-9.3×10^{-2}	-1.2×10^{-1}	-1.1×10^{-1}
0.075	-1.5×10^{-2}	-4.3×10^{-2}	-8.0×10^{-2}	-5.3×10^{-2}
0.050	-1.1×10^{-2}	$+3.8 \times 10^{-2}$	$+6.2 \times 10^{-3}$	$+3.8 \times 10^{-3}$
0.025	-1.4×10^{-5}	$+1.2 \times 10^{-1}$	$+1.0 \times 10^{-1}$	$+1.1 \times 10^{-1}$
0.010	-4.8×10^{-5}	$+2.1 \times 10^{-1}$	$+1.5 \times 10^{-1}$	$+1.5 \times 10^{-1}$

we show the configuration closest to the desired density. Values for the normalized Minkowski functionals B/A and χ/A for the configurations shown in Fig. 3 are listed in Tables V and VI, respectively. These values can be used to describe the predominant phase of each configuration as discussed in Table III.

We now describe the differences between the four systems shown in Fig. 3 for each of the five densities mentioned. This is intended to enlighten the reader about how the equilibration time affects our simulations. We will then discuss the evolution of the Minkowski functionals as a function of density and stretch rate.

1. ***Systems at n*** **= 0.090 fm^{-3}**

At a density of 0.090 fm^{-3} the four systems being compared, first line of Fig. 3, have a negative value for B/A and a positive value for χ/A; see Tables V and VI. This is typical of systems formed mostly by spherical bubbles, see Table III, and it happens because over most of the isosurface defined by n_{th} both principal curvatures are negative, that is, $\kappa_1 < 0$ and $\kappa_2 < 0$. Another thing to notice is how different the simulation that does not include the Coulomb potential looks from the simulations that include Coulomb potential. While the runs that include the Coulomb potential are mostly uniform with several spherical and cylindrical bubbles, the system without Coulomb is formed by two phases: one uniform matter phase and one large spherical bubble. References [42,43] using MD simulations without Coulomb also found two-phase nonuniform structures. These differences can also be noted in the much smaller absolute values for B/A and χ/A for the run without Coulomb system when compared to the others.

Focusing on the simulations that include the Coulomb potential, we note that the one simulation run at constant density has smaller absolute values for B/A and χ/A than the ones obtained from stretching the box; see Tales. V and VI. This is explained by the fact that the bubbles in this system are more elongated than the ones in the systems obtained from stretching the box from a higher density. Also, the simulation ran at a constant density contains some hollow tubes, cylindrical holes that stretch over the whole length of the box, while the others do not. Comparing just the two systems obtained from stretching we observe that the slower the stretch rate the smaller the absolute values for B/A and χ/A. This is because the system stretched at a rate of $\dot{\xi} = 1.0 \times 10^{-7}$ c/fm has had more time to equilibrate and, thus, some of the spherical bubbles that existed in that system at a higher density had enough time to merge and form more elongated bubbles and even some tunnels.

TABLE VI. Values for the normalized Euler characteristic χ/A for our simulations at densities of 0.010, 0.025, 0.050, 0.075, and 0.090 fm^{-3}.

n	χ/A (fm^{-2})			
(fm^{-3})	No Coulomb	Constant	$\dot{\xi} = 10^{-5}$	$\dot{\xi} = 10^{-7}$
0.090	$+5.8 \times 10^{-5}$	$+2.6 \times 10^{-4}$	$+9.0 \times 10^{-4}$	$+7.3 \times 10^{-4}$
0.075	$+1.0 \times 10^{-10}$	-7.1×10^{-4}	$+4.0 \times 10^{-5}$	-4.1×10^{-4}
0.050	$+4.0 \times 10^{-11}$	-1.1×10^{-3}	-7.6×10^{-4}	-1.2×10^{-4}
0.025	$+2.4 \times 10^{-11}$	$+3.4 \times 10^{-4}$	-5.2×10^{-4}	$+0.0 \times 10^{-5}$
0.010	$+2.9 \times 10^{-12}$	$+3.2 \times 10^{-3}$	$+8.0 \times 10^{-4}$	$+1.8 \times 10^{-3}$

2. ***Systems at n*** **= 0.075 fm^{-3}**

As the density decreases to 0.075 fm^{-3} the value of the Euler characteristic χ in the four systems decreased. In the stretched systems this is due to the spherical bubbles merging to form tunnels. In the system run at a constant density the change of sign in χ happens because the system is formed of several interconnected tunnels, the rod-2 b phase in Table III. This also explains its large value of $|\chi/A|$ when compared to the other runs. Again the simulation run without Coulomb potential has only two phases, and the absolute values for both average curvatures is much smaller than in the other simulations.

The configuration obtained from stretching the box quickly, $\dot{\xi} = 1.0 \times 10^{-5}$ c/fm, could be identified by looking up the average curvatures and from Table III as a system of hollow tubes, rod-1 b phase. However, a glance at Fig. 3 shows that is not the case. The system structure, besides hollow tubes, $\chi/A < 0$, contains spherical bubbles, $\chi/A > 0$ and is, thus, a mixture of the sph and rod-2 b structures. As both of these phases contribute similarly to the Euler characteristic χ/A at this density a small value for this quantity is observed; see Eq. (6). This is an indication that this stretch rate is too fast and does not allow enough time for the system to equilibrate.

The simulation that was stretched slowly, $\dot{\xi} = 1.0 \times 10^{-7}$ c/fm, is mainly formed of tunnels that stretch over the whole length of the box. Like the constant-density run it can also be identified as a rod-2 phase, despite their different values for the average curvatures. In this case the smaller absolute value for χ/A implies a lower interconnectivity between the tunnels.

3. ***Systems at n*** **= 0.050 fm^{-3}**

At 0.050 fm^{-3} the run without Coulomb potential exhibits the same behavior it does at 0.075 fm^{-3}. Meanwhile, all simulations with Coulomb interactions change from being mostly concave to mostly convex as show by the change in sign for the values of B/A. The slowly stretched simulation, 1.0×10^{-7} c/fm, has formed sheets that are almost parallel to each other, "lasagna phase", with some connectivity between the slabs. Thus we have the very small value of $|\chi/A|$ when compared to the fast stretched or constant density simulations. The system stretched at a rate of 1.0×10^{-5} c/fm also exhibits plane-like structures. However, since the planes in this system have more connectivity amongst themselves than the slowly stretched system, the value of $|\chi/A|$ is much larger. The constant-density run, though, has much larger values for B/A and $|\chi/A|$ than the stretched systems. The reason is that, unlike the other two stretched systems, this one does not have plane-like structures and is formed of elongated nuclei connected to each other, rod-3 phase. This behavior that produces slab or rod-3 phases depending on the initial condition has already been observed by Schuetrumpf *et al.* in Ref. [16]. As they had already observed, in these two phases the liquid and gas phases have structures that are symmetrical complements of each other.

4. *Systems at* $n = 0.025$ fm^{-3}

At even lower densities, $n = 0.025$ fm^{-3}, the simulation run without Coulomb potential has transitioned to a single liquid phase with nearly flat surfaces that have little curvature. Therefore, both the mean and Gaussian average curvatures B/A and χ/A are very close to zero. The configurations obtained for the other three simulations have similar values for the average mean breadth B/A. This is because the systems with Coulomb interactions are formed of elongated nuclei, known as the “spaghetti phase”, of about the same thickness. However, their values for χ/A differ by large amounts. The reason for this is discussed below.

The configuration obtained by quickly stretching the box has a large negative value for χ/A. This value can be explained by a system made of one large nucleus that splits and reconnects several times, rod-2 phase. Because of the many splits and reconnections the value of χ is negative and large.[1] According to our MST clustering algorithm this system is formed of a nucleus with $A \sim 47\,000$ and about 15 smaller nuclei with mass number in the range of $A = 2$ to $A \sim 2\,000$. On the other hand, the simulation run at constant density has a large positive value for χ/A as it is formed of several elongated nuclei with little to no splits and reconnections. Again using the MST clustering algorithm we see that the final configuration of the constant-density run is formed of 47 nuclei with mass number A in the range of $A \sim 150$ to $A \sim 3200$. In between these two extremes is the system obtained from slowly stretching the box which has a value for χ/A close to zero. Because of periodic boundary conditions, this system is formed by only three large spaghetti-like nuclei with $A \sim 7000$, 17 000, and 27 000. Since these nuclei do not curve or split/reconnect and are for the most part parallel to each other, one of its principal curvatures will always be close to zero. Thus, we have the small value for χ/A for the slowly stretched system when compared to the other two systems.

5. *Systems at* $n = 0.010$ fm^{-3}

At a density of 0.010 fm^{-3} both the system obtained from slowly stretching, $\dot{\xi} = 1.0 \times 10^{-7}$ c/fm, and the system obtained from constant-density equilibration exhibit only (almost) spherical nuclei. This is known as the “gnocchi phase”. Meanwhile, the system stretched at a fast rate $\dot{\xi} = 1.0 \times 10^{-5}$ c/fm exhibits spherical nuclei as well as elongated nuclei. Finally, for the simulation without Coulomb interactions, the single liquid phase now occupies a smaller fraction of the total simulation volume than at a density of 0.025 fm^{-3}. These differences can be seen from the configurations shown in the last row of Fig. 3.

In order to quantify some of the differences between the low density systems we use our MST and MSTE algorithms to determine the size of clusters present in the different simulations at densities of $n = 0.010$ fm^{-3} and less. In Fig. 4

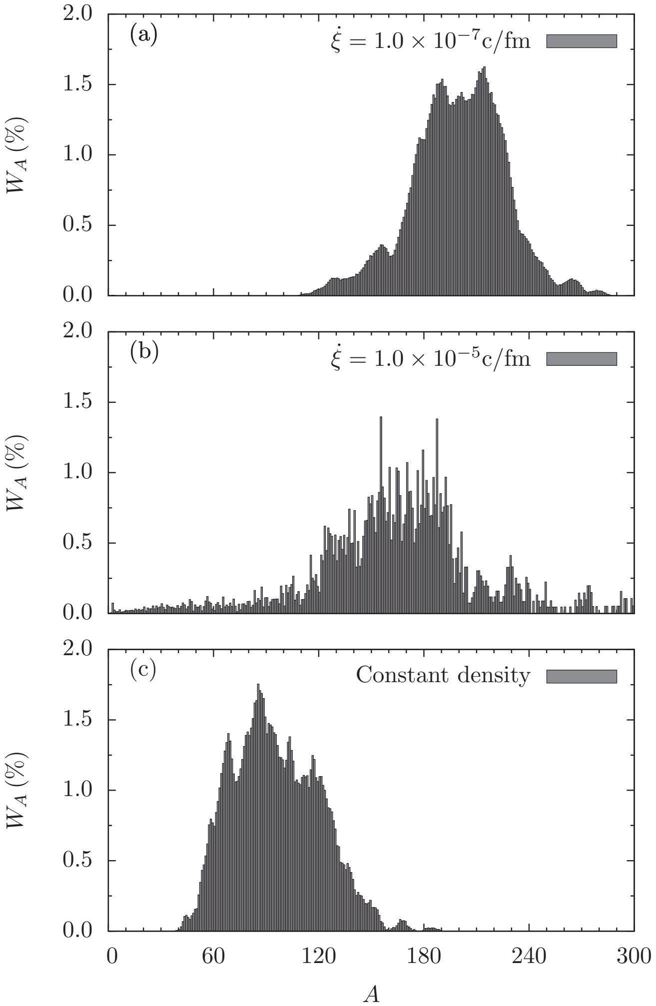

FIG. 4. Mass fraction W_A obtained from the MST algorithm discussed in Sec. II C. W_A is the mass fraction of the system composed of nuclei with mass number A at a densities of 0.010 fm^{-3} and less for three different runs: one from (a) stretching the box at a rate $\dot{\xi} = 1.0 \times 10^{-7}$ c/fm, one obtained from (b) stretching the box at $\dot{\xi} = 1.0 \times 10^{-5}$ c/fm, and, finally, one obtained from (c) letting the system equilibrate at a constant density.

---

[1] To understand this better we recall that an orientable surface R has an Euler characteristic given by $\chi(R) = 2 - 2g(R)$. Here $g(R)$ is the genus of that surface, that is, the number of “handles” in the surface. Thus, while a nucleus in empty space with $g(R) = 0$, or a cavity in uniform matter also with $g(R) = 0$, has $\chi = 2$, a torus with $g(R) = 1$ has $\chi = 0$ and a double-torus or “pretzel” with $g(R) = 2$ has $\chi = -2$.

we plot the mass fraction

$$W_A = \frac{N_A M_A}{M_{\rm tot}} \tag{10}$$

of the system that is formed by clusters with nuclear number A obtained with the MST algorithm. Above, $M_{\rm tot} = \sum_A N_A M_A$ is the total mass of the system, N_A is the number of clusters with mass number A, and mass $M_A = AM_N$. We recall that the nucleon mass is set to $M_N = 939$ MeV. For the stretched systems, Figs. 4(a) and 4(b), we plot W_A averaged over configurations with densities of $n = 0.010$ fm^{-3} and less. For the constant density run, Fig. 4(c), we plot W_A averaged over the last one-third of the run.

We now discuss the difference in results for the systems and, in the end of this section, the results obtained from the MSTE algorithm. First we note that, due to the classical nature of our simulation, protons and neutrons are often knocked out of a cluster and end up being absorbed by another cluster. This leads to nuclei not being of constant size throughout the simulation even though no major topological phase transition happens at $n \lesssim 0.010$ fm^{-3}.

Figures 4(a) and 4(c) show us that there is a significant difference in the size of the spherical nuclei formed in the slowly stretched system and in the simulation at a constant density. While the system stretched at $\dot{\xi} = 1.0 \times 10^{-7}$ c/fm has in its final configuration about 260 spherical nuclei with atomic numbers in the range of $A \sim 120$ to 300, the final constant-density run configuration has about 550 nuclei mostly in the range $A \sim 40$ to 150. We note that there are barely any free neutrons in these systems and, therefore, the mass number and charge are related by $A \sim 5Z/2$. Meanwhile, the system stretched at a fast rate $\dot{\xi} = 1.0 \times 10^{-5}$ c/fm exhibits about 650 nuclei in its final configuration. Figure 4(b) shows that most of these nuclei are spherical nuclei of small to large sizes, A from 1 to ~300, while a few are elongated nuclei, $A \gtrsim 300$ (not shown). The largest nuclei for the final configuration of the system expanded at $\dot{\xi} = 1.0 \times 10^{-7}$ c/fm has $A \sim 1000$.

As mentioned, the system obtained from stretching the box at a slow rate has very few small nuclei $A \lesssim 10$, while most have mass number in the range $A \sim 120$ to 300. Also, the nuclei form a solid-like structure, possibly a bcc lattice. One of the planes of the lattice can be seen clearly in Fig. 5. A reason to believe the lattice has a bcc structure is its temperature T, average charge $\langle Z \rangle$, and the ratio $\kappa = a/\lambda$ of the inter-ion spacing a to screening length λ. At 0.010 fm^{-3} the system has an average of $\langle Z \rangle \simeq 78$, temperature of 1 MeV and inter-ion spacing $a = (3/4\pi n_{\rm ion}) \simeq 16.7$ fm. The ion density $n_{\rm ion}$ is obtained from $n_{\rm ion} = Y_p n/\langle Z \rangle$. Thus, $\kappa \simeq 1.67$ and the Coulomb parameter Γ is

$$\Gamma = \frac{\langle Z \rangle^2 e^2}{aT} \simeq 530. \tag{11}$$

According to Fig. 1 of Ref. [44] a system with these parameters should form a bcc lattice, provided we ignore the free energy of mixing of ions of different charges [45]. We note here that the definitions of κ and λ in Ref. [44] are slightly different from ours. Vaulina *et al.* define $a = n^{-1/3}$ so our value of κ (Γ) should be multiplied (divided) by a factor of $(3/4\pi)^{1/3}$ in order to be compared to theirs. This, however, does not change our conclusion.

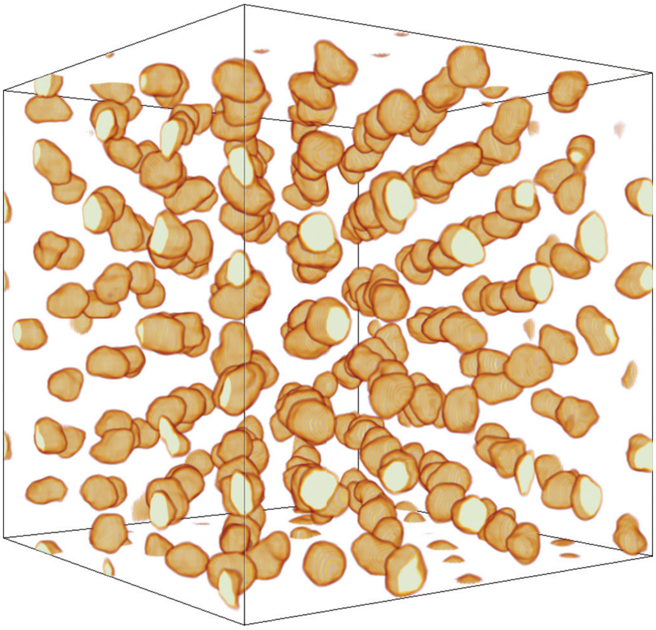

FIG. 5. (Color online) System at a density of 0.010 fm^{-3} obtained from stretching the box at a rate of $\dot{\xi} = 1.0 \times 10^{-7}$ c/fm from 0.10 fm^{-3}. The golden surfaces represent isosurfaces of charge density with $n_{\rm ch} = 0.03$ fm^{-3} while the cream color shows regions such that $n_{\rm ch} > 0.03$ fm^{-3}. The system is shown at an angle that makes it easier to see that the nuclei form some type of lattice. This figure was generated using PARAVIEW [41].

The system obtained from a random start and evolved at constant density also has very few small nuclei $A \lesssim 10$, while most nuclei are in the range $A \sim 40$ to 150; see the bottom plot of Fig. 4. The nuclei in this sytem do not form a lattice structure, but rather form a liquid-like structure as its average charge $\langle Z \rangle = 35.7$ implies a value of $\Gamma \simeq 142$ and $\kappa \simeq 1.29$. Clear differences between this system and the one generated from slowly stretching the box can be seen by comparing Figs. 5 and 6. The system run at constant density forms smaller nuclei than the slowly stretched system because of the effects of the Coulomb barrier. From their initial random positions nucleons start to correlate to form nuclei. However, as they group together the charge of the nuclei they form reaches a value that makes it increasingly difficult for other small nuclei to merge with it. This may be a disadvantage of treating the system classically because quantum tunneling is neglected.

Unlike the two systems just discussed at 0.010 fm^{-3}, the configuration obtained from stretching the box at a rate of $\dot{\xi} = 1.0 \times 10^{-5}$ c/fm has both several small nuclei $A \lesssim 20$ and some large elongated nuclei, $A \gtrsim 300$ with a peak in mass number of $A \sim 150$, see the Fig. 4(b). This difference arises because this system did not have enough time to equilibrate. The large elongated nuclei have not had time to fission into smaller nuclei. It is likely that the equilibration time for the pasta structures shown here is much larger than the very roughly $t \approx 100\,000$ fm/c time scale for significant

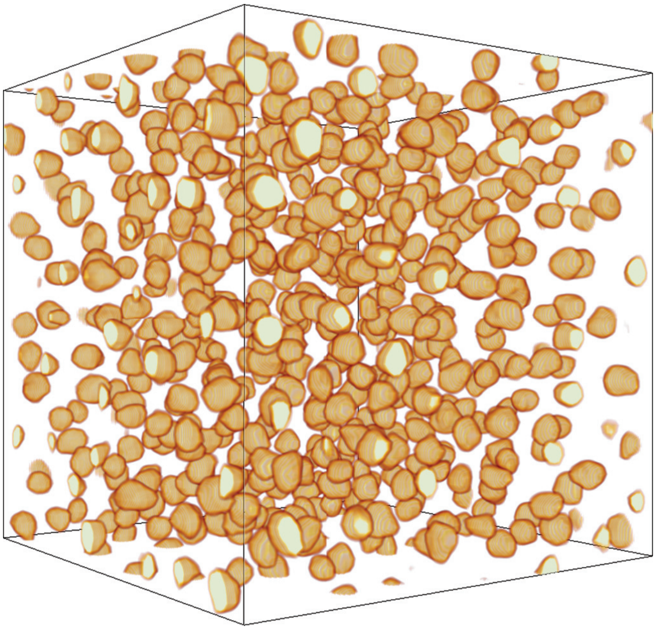

FIG. 6. (Color online) System at a density of 0.010 fm^{-3} obtained from an initial random configuration of protons and neutrons at the same density. The golden surfaces represent isosurfaces of charge density with $n_{\mathrm{ch}} = 0.03\ \mathrm{fm}^{-3}$ while the cream color shows regions such that $n_{\mathrm{ch}} > 0.03\ \mathrm{fm}^{-3}$. The system is shown from the same angle as Fig. 5. This figure was generated using PARAVIEW [41].

density changes in a system stretching at a rate of $\dot{\xi} = 1.0 \times 10^{-5}\ c/\mathrm{fm}$.

All of the analysis above focused solely on the size of nucleon clusters obtained using the MST algorithm. For completeness, in Fig. 7 we compare the results of the mass fraction W_A obtained from the MST and the MSTE algorithms for the system expanded at a rate of $\dot{\xi} = 1.0 \times 10^{-7}\ c/\mathrm{fm}$. As shown in Fig. 7(a) the MSTE algorithm detects a significant fraction of very small sized nuclei, $A \lesssim 5$, that are not observed by the MST algorithm. These small nuclei are mostly formed by nucleons that are at the surface of large clusters and, because of their large relative momenta with respect to the overall cluster, are not seen as bound by the MSTE algorithm. These are most likely nucleons that are in the process of being knocked out or absorbed by a larger cluster. Another feature observed in Fig. 7(a) is that the mass fractions W_A obtained from the MST and MSTE for large nuclei are very similar, though the former one seems to be shifted towards large A. This becomes clear in Fig. 7(b), when we shift the mass fraction distribution by three nucleon units, $A \to A - 3$. Now both distributions seem close to identical. A ratio between the mass fraction distributions W_{A-3}^{MST} obtained from the MST algorithm shifted by three nucleons and W_A^{MSTE} obtained from the MSTE algorithm is shown in Fig. 7(c). Note that this ratio is within 10% of unity for the region that describes most of the mass of the system, $A \sim 120$ to ~ 250. Although the results for cluster distribution found by both algorithms are similar, the MST algorithm yields a much better agreement to the number of topological structures in the system given by the value of χ. This is because some nucleons seen as free by the MSTE algorithm still are within the isosurface defined by $n = n_{\mathrm{th}}$ that defines the topology of the system.

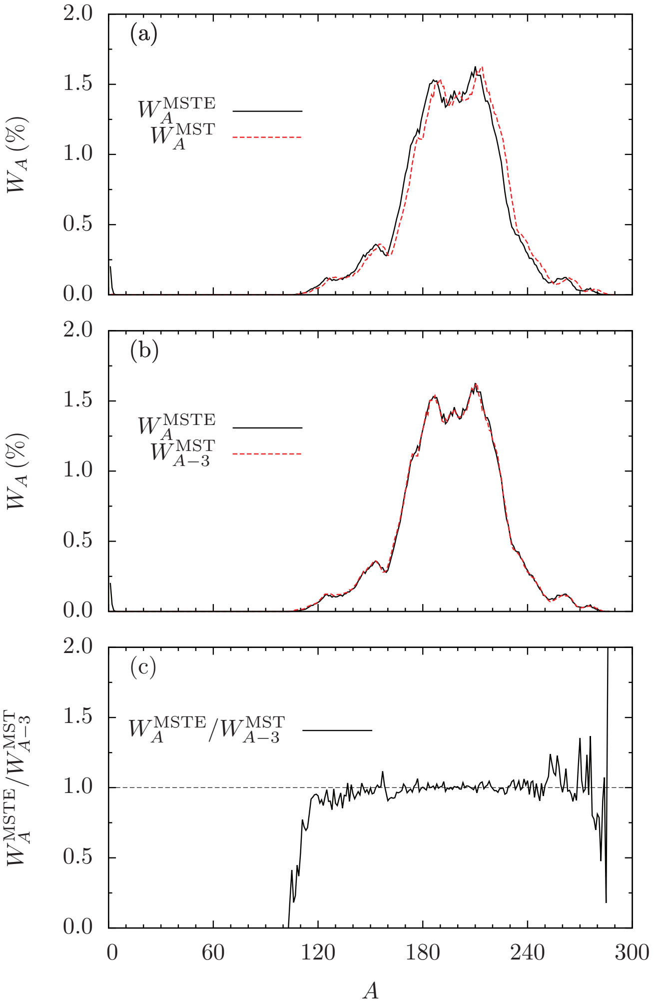

FIG. 7. (Color online) (a) The mass fractions W_A^{MST} and W_A^{MSTE} obtained from the MST and MSTE algorithms discussed in Sec. II C. W_A is the percentage of the system that is composed of nuclei with mass number A for the system stretched at a rate of $\dot{\xi} = 1.0 \times 10^{-7}\ c/\mathrm{fm}$ when at a density of 0.010 fm^{-3} or less. (b) The same as (a) with the mass fraction W_A^{MST} shifted by 3 nucleon units, $A \to A - 3$. (c) The ratio between W_A^{MSTE} and W_{A-3}^{MST}.

6. *Simulation visualizations*

Movies that show charge density isosurfaces versus density for the simulations described in the text are available online (see Supplemental Material [46]). A description of the movies can be found in Table VII.

7. *Minkowski functionals*

The evolution of the normalized mean breadth B/A and Euler characteristic χ/A as a function of the density n for three runs done using different stretching rates, $\dot{\xi} = 1.0 \times 10^{-5}$, 1.0×10^{-6}, and $1.0 \times 10^{-7}\ c/\mathrm{fm}$, are shown in Figs. 8 and 9, respectively. Also shown in these figures are the results obtained for the constant-density runs at 0.010, 0.025, 0.050,

TABLE VII. Description of movies of simulations described in the text. First column lists the file names, the second one the stretching rate of the simulation, and the third column lists the file size in MB. Visualizations files were generated using PARAVIEW software [41].

File	$\dot{\xi}$ (c/fm)	Size (MB)
1e-7_720.avi	1.0×10^{-7}	90.8
1e-6_720.avi	1.0×10^{-6}	90.8
1e-5_720.avi	1.0×10^{-5}	45.8
1e-6_720_no_coulomb.avi	1.0×10^{-6}[a]	27.9

[a] Does not include the Coulomb potential.

0.075, and 0.090 fm^{-3} and for a stretching run with $\dot{\xi} = 1.0 \times 10^{-6}$ and no Coulomb interactions.

First we note that, by comparing the systems that include and do not include the Coulomb potential, it becomes clear that it is the competition between nuclear and Coulomb forces that gives rise to the richness of the pasta shapes. Without this competition the shapes accessible to the pasta phase are very limited, as noted by the small values for the normalized Minkowski functionals for the simulation that does not include the Coulomb potential.

We also note that systems stretched at rates $\dot{\xi}$ of 1.0×10^{-5} and 1.0×10^{-6} c/fm do not have enough time to equilibrate, so that the transitions between shapes are not as sharp as in the system stretched at $\dot{\xi} = 1.0 \times 10^{-7}$ c/fm. If the system is stretched slowly enough, $\dot{\xi} = 1.0 \times 10^{-7}$ c/fm, the pasta shapes have more time to equilibrate and the transitions between shapes are more abrupt.

In the plot shown in Fig. 8 for the normalized mean breadth B/A we see that the faster a system is stretched the smoother is the mean breadth dependence on the density n. For a stretch rate of $\dot{\xi} = 1.0 \times 10^{-5}$ c/fm, B/A increases almost linearly as the density decreases. If the expansion rate is decreased to $\dot{\xi} = 1.0 \times 10^{-6}$ c/fm some kinks in the curve of B/A appear. The two most prominent ones are at 0.040 fm^{-3}, the transition region from the lasagna to the spaghetti phase, and 0.015 fm^{-3}, the transition region from the spaghetti to the gnocchi phase.

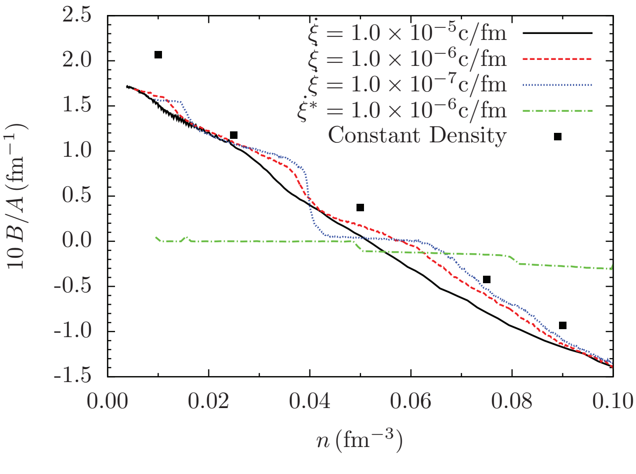

FIG. 8. (Color online) Normalized mean breadth B/A as a function of the density n for three complete calculations using stretch rates $\dot{\xi} = 10^{-5}$, 10^{-6}, and 10^{-7} c/fm and one calculation with stretch rate $\dot{\xi}^* = 10^{-6}$ c/fm ignoring Coulomb interactions. Results are compared to five computations done at constant densities of 0.010, 0.025, 0.050, 0.075, and 0.090 fm^{-3}.

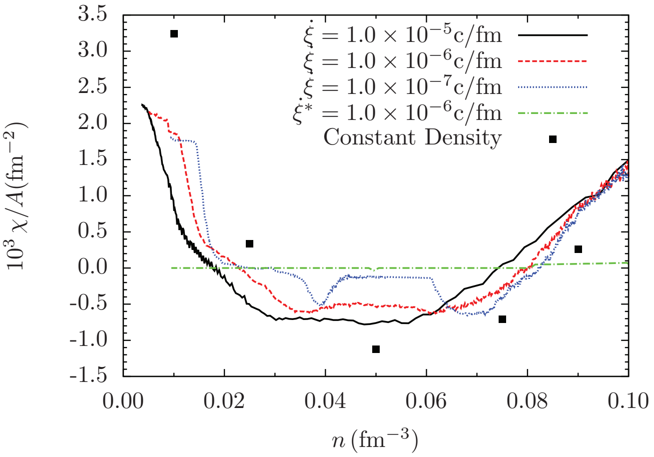

FIG. 9. (Color online) Lines represent the normalized Euler characteristic χ/A as a function of the density n for three complete calculations using stretch rates $\dot{\xi} = 10^{-5}$, 10^{-6}, and 10^{-7} c/fm and one calculation with stretch rate $\dot{\xi}^* = 10^{-6}$ c/fm ignoring Coulomb interactions. Results are compared to five computations done at constant densities of 0.010, 0.025, 0.050, 0.075, and 0.090 fm^{-3}.

When the expansion rate is decreased further, $\dot{\xi} = 1.0 \times 10^{-7}$ c/fm, the kinks in the curve of B/A become even larger and are displaced to slightly higher densities. The mean breadth B in the region from 0.040 fm^{-3} to 0.060 fm^{-3} is close to zero indicating that the pasta shapes have almost zero curvature in all directions. This is characteristic of the lasagna phase as it is formed of nearly flat sheets of nuclear matter. At a density of 0.040 fm^{-3} the transition region from the lasagna to the spaghetti phase becomes even sharper than before. Also, the transition from the spaghetti to the gnocchi phase happens at a higher density, 0.015 fm^{-3}, than for the system stretched at $\dot{\xi} = 1.0 \times 10^{-6}$ c/fm, 0.012 fm^{-3}.

Figure 9 shows the normalized Euler characteristic χ/A as a function of density n. We note again that the curves become smoother as the expansion rate increases, thus showing the system does not have time to reach equilibrium when stretched too fast. In this plot the transitions from the spaghetti to the gnocchi phase becomes clearer for the slowest expansion rate. Another important thing to note is that, when looking at both plots, it is clear that for lower densities the topologies of the systems obtained from expansion runs do not converge to the values obtained from the constant-density runs. This suggests that the constant-density runs (at least) have not equilibrated.

IV. CONCLUSIONS

In this paper we studied the dynamics of pasta phase transitions using an MD formalism to isothermally expand nuclear matter from densities of 0.100 fm^{-3} to 0.010 fm^{-3} or less. Expansions were performed at a temperature of $T = 1$ MeV and proton fraction of $Y_p = 0.40$ using stretching rates of $\dot{\xi} = 10^{-5}$, 10^{-6}, and 10^{-7} c/fm; see Eq. (5). These runs were then compared to constant-density runs at densities of 0.010, 0.025, 0.050, 0.075, and 0.090 fm^{-3}.

For each run we obtained the Minkowski functionals as a function of density and learned that, for MD simulations such as ours, the methods used to prepare the pasta alter the resulting pasta shapes significantly. First, we noticed that the Coulomb force is essential for the formation of pasta-like configurations. Without the Coulomb force, the pasta shapes are confined to small values of both the mean breadth B and Euler characteristic χ.

When the Coulomb potential is included, we obtain pasta configurations similar to the ones obtained by other works using several other methods as discussed in Sec. I. These shapes are spherical holes, cylindrical holes, sheets (lasagna), cylinders (spaghetti), and spheres (gnocchi). However, the geometrical shapes accessible to the pasta phases in our simulations as well as their arrangement were dependent on the expansion rates. In the simulation with the slowest expansion rate, $\dot{\xi} = 10^{-7}$ c/fm, nearly periodic structures are formed in the gnocchi, spaghetti, and lasagna phases in addition to the periodicity imposed by the periodic boundary conditions. Meanwhile the pasta shapes obtained from fast expansion rates, $\dot{\xi} = 10^{-5}$ and 10^{-6} c/fm, did not exhibit any additional translational symmetry beyond the enforced ones. We recall here that calculations that used volumes larger than the Wigner-Seitz cell obtained these additional translational symmetries for the pasta shapes [12,23–26] which had not been observed by the larger MD calculations of Horowitz *et al.* [6,7,27,28].

Another point to note is that the two simulations with fastest expansion rates have not reached equilibrium. This can be argued from the fact that the faster the expansion rate the longer, as a fraction of total run time, different pasta phases coexisted. However, for the slow expansion rate, the coexistence of pasta shapes did not last as long, as a fraction of total run time. Thus, for fixed temperature and proton fraction, as the expansion rate gets closer to being quasistatic the transition between phases become more abrupt. This suggests that the transition between different pasta phases is first-order. The plots of B/A and χ/A for the slowest expansion run show that the transitions between lasagna to spaghetti and spaghetti to gnocchi phases are much sharper than in the fast expansion runs.

The sudden changes in pasta shapes, B/A and χ/A, as the density of the system is decreased can help us place lower limits on the density where each pasta phase occurs. Because of the way the system is evolved a pasta phase may be kept in a metastable state at a lower density than it would normally exist. By this reasoning we claim that for a proton fraction of $Y_p = 0.40$ and temperature $T = 1$ MeV the lasagna phase occurs for densities of $n \simeq 0.040$–0.060 fm^{-3}. The spaghetti phase occurs for densities of $n \simeq 0.018$–0.40 fm^{-3} while the gnocchi phase occurs below a density of 0.018 fm^{-3}.

These simulations also set a time scale for the transition between the lasagna/spaghetti phases and the spaghetti/gnocchi phases. The transition from gnocchi to spaghetti phase happens in the range $n \simeq 0.0145$–0.018 fm^{-3} and takes a time of approximately 1 300 000 fm/c. Meanwhile, the transition from spaghetti to lasagna phase happens at $n \simeq 0.038$–0.044 fm^{-3}, and takes a time of approximately 600 000 fm/c.

In Ref. [26] Watanabe *et al.* obtained the transition time using QMD from adiabatic compression runs starting at a temperature of $T = 0.25$ MeV for the transition between the spherical (gnocchi) and cylindrical (spaghetti) phases for a similar proton fraction, $Y_p = 0.39$. In their work, the transition between these two phases happened at $n \simeq 0.040$–0.045 fm^{-3} and the transition time was of the order of 10 000 fm/c. This much shorter transition time may be because of the momentum-dependent QMD interactions that may increase the nucleon momenta in comparison to our momentum-independent interactions. Furthermore some of the difference in transition time may arise because the QMD simulations were for significantly smaller systems using fewer nucleons than the 51 200 that we use.

We also observed that constant-density runs with nucleons initially assigned random positions exhibit some pasta-like shapes such as cylindrical holes, cylinders, and spheres. These runs, however, were not able to produce spherical holes and flat sheets as the expansion runs did. It is likely that the spherical-hole phase appears at higher density for this type of simulation while the lasagna phase may take a very long time to form from the initial conditions chosen. Also, for the low density run, $n = 0.010$ fm^{-3}, the Coulomb barrier and the classical character of our simulation prevented the formation of large nuclei.

Our simulations explicitly demonstrate nucleation mechanisms for each of the observed pasta phase transitions. First spherical holes were observed to nucleate from density fluctuations in an originally uniform system. This is very similar to the nucleation of vapor bubbles for a conventional liquid-gas phase transition. However, the Coulomb interaction keeps the spherical holes from growing to very large sizes, as occurred in our simulation without Coulomb interactions.

These spherical holes were observed to merge, with a further decrease in density, to form cylindrical holes ("anti-spaghetti"). Next the anti-spaghetti became cross-linked and finally quickly merged to form the lasagna phase. As the density was decreased still further, holes appeared in the lasagna planes and these holes grew to convert the lasagna into a cross-linked network of spaghetti. These holes, in the cross-linked network of spaghetti, lead to a negative excursion in χ/A shown in Fig. 9 near $n = 0.04$ fm^{-3} for the run with $\dot{\xi} = 10^{-7}$ c/fm. The cross-links disappeared at lower density to produce isolated nearly straight spaghetti strands. Finally, at even lower densities these spaghetti strands rapidly fissioned to form nearly spherical nuclei.

If the transition, with changing density, from spaghetti to spherical nuclei is reversible, then the criteria for the first formation of nonspherical pasta phases is related to when the spaghetti strands become unstable to fission. This depends on the sizes of the Coulomb and surface energies. Thus pasta formation is related to nuclear fission.

In future work we will perform simulations with even slower expansion rates starting above saturation density to further determine when the pasta is equilibrated. Once the pasta is equilibrated we may study the observed low energy bending modes of the spaghetti and lasagna shapes that may contribute significantly to the heat capacity even at low temperatures.

In addition, we will explore finite size effects by performing larger simulations with more than 51 200 nucleons. Finally, we will perform simulations with a range of smaller proton fractions. These simulations will then be used to calculate a variety of observables. Neutrino opacities can be determined using the formalism in Refs. [6,7] while the bulk viscosity may be obtained by homogeneous periodic compressions and expansions of the system [47]. We also intend to determine the shear modulus and breaking strain of the pasta phases by observing the response of the system to deformations of the simulation volume.

ACKNOWLEDGMENTS

We are grateful to David Reagan at the Advanced Visualization Laboratory, Indiana University for his help with PARAVIEW. We would also like to thank Indiana University for access to the BigRed supercomputer. This research was supported in part by DOE Grants No. DE-FG02-87ER40365 (Indiana University) and No. DE-SC0008808 (NUCLEI SciDAC Collaboration) and by the National Science Foundation through XSEDE resources provided by the National Institute for Computational Sciences under Grant No. TG-AST100014.

[1] G. Baym, H. A. Bethe, and C. J. Pethick, Nucl. Phys. A **175**, 225 (1971).
[2] R. Williams and S. Koonin, Nucl. Phys. A **435**, 844 (1985).
[3] C. Pethick and A. Potekhin, Phys. Lett. B **427**, 7 (1998).
[4] G. Watanabe, K. Iida, and K. Sato, Nucl. Phys. A **676**, 455 (2000).
[5] D. Q. Lamb, J. M. Lattimer, C. J. Pethick, and D. G. Ravenhall, Phys. Rev. Lett. **41**, 1623 (1978).
[6] C. J. Horowitz, M. A. Pérez-García, and J. Piekarewicz, Phys. Rev. C **69**, 045804 (2004).
[7] C. J. Horowitz, M. A. Pérez-García, J. Carriere, D. K. Berry, and J. Piekarewicz, Phys. Rev. C **70**, 065806 (2004).
[8] D. G. Ravenhall, C. J. Pethick, and J. R. Wilson, Phys. Rev. Lett. **50**, 2066 (1983).
[9] M. aki Hashimoto, H. Seki, and M. Yamada, Prog. Theor. Phys. **71**, 320 (1984).
[10] N. Gupta and P. Arumugam, Phys. Rev. C **87**, 028801 (2013).
[11] K. Nakazato, K. Oyamatsu, and S. Yamada, Phys. Rev. Lett. **103**, 132501 (2009).
[12] M. Okamoto, T. Maruyama, K. Yabana, and T. Tatsumi, Phys. Lett. B **713**, 284 (2012).
[13] P. Magierski and P.-H. Heenen, Phys. Rev. C **65**, 045804 (2002).
[14] F. Grill, C. Providência, and S. S. Avancini, Phys. Rev. C **85**, 055808 (2012).
[15] W. G. Newton and J. R. Stone, Phys. Rev. C **79**, 055801 (2009).
[16] B. Schuetrumpf, M. A. Klatt, K. Iida, J. A. Maruhn, K. Mecke, and P.-G. Reinhard, Phys. Rev. C **87**, 055805 (2013).
[17] H. Pais and J. R. Stone, Phys. Rev. Lett. **109**, 151101 (2012).
[18] T. Maruyama, T. Tatsumi, D. N. Voskresensky, T. Tanigawa, and S. Chiba, Phys. Rev. C **72**, 015802 (2005).
[19] S. S. Avancini, D. P. Menezes, M. D. Alloy, J. R. Marinelli, M. M. W. Moraes, and C. Providência, Phys. Rev. C **78**, 015802 (2008).
[20] T. Maruyama, K. Niita, K. Oyamatsu, T. Maruyama, S. Chiba, and A. Iwamoto, Phys. Rev. C **57**, 655 (1998).
[21] G. Watanabe, K. Sato, K. Yasuoka, and T. Ebisuzaki, Phys. Rev. C **66**, 012801 (2002).
[22] G. Watanabe, K. Sato, K. Yasuoka, and T. Ebisuzaki, Phys. Rev. C **68**, 035806 (2003).
[23] G. Watanabe, K. Sato, K. Yasuoka, and T. Ebisuzaki, Phys. Rev. C **69**, 055805 (2004).
[24] H. Sonoda, G. Watanabe, K. Sato, K. Yasuoka, and T. Ebisuzaki, Phys. Rev. C **77**, 035806 (2008).
[25] G. Watanabe, T. Maruyama, K. Sato, K. Yasuoka, and T. Ebisuzaki, Phys. Rev. Lett. **94**, 031101 (2005).
[26] G. Watanabe, H. Sonoda, T. Maruyama, K. Sato, K. Yasuoka, and T. Ebisuzaki, Phys. Rev. Lett. **103**, 121101 (2009).
[27] C. J. Horowitz, M. A. Pérez-García, D. K. Berry, and J. Piekarewicz, Phys. Rev. C **72**, 035801 (2005).
[28] C. J. Horowitz and D. K. Berry, Phys. Rev. C **78**, 035806 (2008).
[29] J. Piekarewicz and G. T. Sánchez, Phys. Rev. C **85**, 015807 (2012).
[30] C. O. Dorso, P. A. Giménez Molinelli, and J. A. López, Phys. Rev. C **86**, 055805 (2012).
[31] J. A. Pons, D. Viganò, and N. Rea, Nat. Phys. **9**, 431 (2013).
[32] C. J. Horowitz and K. Kadau, Phys. Rev. Lett. **102**, 191102 (2009).
[33] C. Lang, J. Ohser, and R. Hilfer, J. Microsc. **203**, 303 (2001).
[34] K. Michielsen and H. D. Raedt, Phys. Rep. **347**, 461 (2001).
[35] A. L. Fetter and J. D. Walecka, *Quantum Theory of Many-Particle Systems* (McGraw-Hill, New York, 1971).
[36] L. Verlet, Phys. Rev. **159**, 98 (1967).
[37] B. L. Holian and D. E. Grady, Phys. Rev. Lett. **60**, 1355 (1988).
[38] A. Strachan and C. O. Dorso, Phys. Rev. C **56**, 995 (1997).
[39] C. Dorso and J. Randrup, Phys. Lett. B **301**, 328 (1993).
[40] National Institute for Computational Sciences, University of Tennessee, and Oak Ridge National Laboratory.
[41] A. Henderson, *Para View Guide, A Parallel Visualization Application* 2007, http://www.paraview.org/.
[42] K. Binder, B. J. Block, P. Virnau, and A. Tröster, Am. J. Phys. **80**, 1099 (2012).
[43] C. Dorso, P. Molinelli, J. Nichols, and J. López, arXiv:1211.5582.
[44] O. Vaulina, S. Khrapak, and G. Morfill, Phys. Rev. E **66**, 016404 (2002).
[45] Z. Medin and A. Cumming, Phys. Rev. E **81**, 036107 (2010).
[46] See Supplemental Material at http://link.aps.org/supplemental/10.1103/PhysRevC.88.065807 for movies of the simulations.
[47] W. G. Hoover, A. J. C. Ladd, R. B. Hickman, and B. L. Holian, Phys. Rev. A **21**, 1756 (1980).